Indian J Phys (September 2024) 98(10):3571–3582
https://doi.org/10.1007/s12648-024-03147-x

ORIGINAL PAPER

Exploring electronic, structural, optical, and elastic properties of MgX_2O_6 (x = Ta, Nb) compounds for photovoltaic and optoelectronic applications: first study effort

M Aycibin[1,3]*, M Çelebi[1,2], M Erzen[1,2] and H Akkuş[1]

[1]Department of Physics, Faculty of Science, Van Yuzuncu Yil University, Van, Turkey

[2]Department of Physics, Institute of Natural and Applied Sciences, Van Yuzuncu Yil University, 65080 Van, Turkey

[3]Department of Medical Services and Techniques, Vocational School of Technical Sciences, Mersin University, 33334 Mersin, Turkey

Received: 12 June 2023 / Accepted: 25 February 2024 / Published online: 18 July 2024

Abstract: In this study, the structural, optical, and elastic properties of tetragonal $MgTa_2O_6$ and orthorhombic $MgNb_2O_6$ were determined using the Wien2k and ABINIT computational programs with the aid of density functional theory. The results imply that both compounds are classified as wide band gap semiconductor with 4.143 eV (for $MgTa_2O_6$) and 3.653 eV (for $MgNb_2O_6$) with PBEsol-GGA + TB-mBJ approximation. The findings of bulk modulus, shear modulus, Young modulus, Poisson's ratio, and anisotropy factors were determined and discussed in detail. The ductile behavior and the mechanism of structural stability were also explained.

Keywords: AB_2O_6; Density functional theory; Elastic properties; Direct transition; Optical anisotropy

Introduction

Materials with AB_2O_6-type structures have attracted researcher's attention due to their physical properties and have been subjected to many investigations [1–3]. In particular, compounds with the elements Ta and Nb, which are known for their photocatalytic and microwave dielectric properties, have been the focus of researchers [4–7].

In 1968, Emmenegger used crystal growth experiments to produce single crystals including MgX_2O_6 (X = Ta, Nb) (hereafter MXO) [8]. Greenblatt and his coworkers grew MNb_2O_6 (M = Mg, Zn, Ba) crystals from $Na_2B_4O_7$ and $Cs_2B_4O_7$ powder [9]. Blasse et al. reported the preparation of the process of $MgNb_2O_6$ (MNO) with higher efficiency [10]. They showed that the compound has an orthorhombic structure. MNO with orthorhombic structure was prepared by solid-state and solution techniques [11]. Higuchi et al. used the floating zone method to grow $MgTa_2O_6$ (MTO) single crystals and investigate the optical properties of the compound [12]. The Czochralski method was used to grow MNO single crystals and study their optical properties [13]. Mcbride and coworkers used the element Ni as a dopant to dope the MNO compound, which was grown by the flame fusion method [14]. After the doping process, they measured the luminescence and absorption properties of the compound. MNO was obtained via a modified mixed oxide synthetic route and analyzed by Ananta, Brysdson, and Thomas [15]. Kim investigated the structure of MNO and $Pb(Mg_{1/3}Nb_{2/3})O_3$ as a function of working temperature [16]. Sreedhar and Mitra used MNO to obtain $Pb_3MgNb_2O_9$ and analyzed the compound obtained [17]. Pure MNO with high surface area and crystallinity was obtained by Emerson et al. [18] by the polymerized complex method. Gd-doped MNO single crystals were investigated using an electron paramagnetic resonance [19]. The MTO powder was prepared to analyze the particle size [5]. Tealdi and coworkers used MTO as a host material to measure its defects and doping properties [4]. Huang et al. investigated the effects of adding CuO on the dielectric properties of MTO in the microwave region [7]. The mechanochemical synthesis method was used to prepare MTO powder [20]. Zhang et al. used the citrate solgel method to prepare MTO and MNO nanopowders [21, 22]. The molten salt method was used to obtain a new form of MTO and MNO [23–25]. MNO and MTO were prepared using the conventional solid-state ceramic route to reveal

*Corresponding author, E-mail: murataycibin@mersin.edu.tr

their structure by different techniques [26]. The luminescence and structural properties of MNO, prepared by the solgel method, were investigated [27]. The microwave dielectric properties of MXO (X = Ta, Nb) ceramics with and without the addition of dopants were investigated [28–35]. Si et al. used the solid-state reaction method to synthesize and measure the photoluminescence spectra of MNO-based phosphors [36]. The ZnS/MNO heterostructure was investigated for its structural and optical properties [37]. The luminescence properties of MTO prepared by solid-state chemical reaction were stimulated [38]. Birdeanu, Vaida, and Fagadar-Cosma used hydrothermal methods to synthesize ZXO and MXO pseudo-binary oxide materials [39]. Miller and Rondinelli used DFT calculation to reveal a carrier-controlled metal–insulator transition (MIT) in trirutile MTO [40]. The optical properties of MTO grown by the optical floating method were carried out [41]. Basavaraju et al. conducted research that considered the product MNO and analyzed its application for photocatalytic degradation and electronic sensor studies [42]. MNO was used as a host material and doped with different elements to measure its luminescent and thermal properties [43, 44].

As we have seen above, except one study revealing a carrier-driven metal–insulator transition (MIT) in MTO, no computational studies of these compounds have been performed to date. It is well known that knowledge of the electronic structure of solids plays a crucial role in understanding their physical and chemical properties. Moreover, it is important to know these properties of compounds before considering them for technological applications. Therefore, this work was dedicated to the investigation of the electronic, structural, optical, elastic, and dynamic properties of MXO compounds for potential optoelectronic applications and to fill a gap in the literature.

Computation details

While MTO crystallizes in the space group P42/mnm (No.136) with a = b = 4.65 Å and c = 9.07 Å [4, 45–47], the structure of MNO is orthorhombic (Pbcn (60)) with a = 14.465 Å, b = 5.812 Å, and c = 5.132 Å [15, 42, 48] (Fig. 1). Two different approaches, namely Wien2k [49] and ABINIT [50], were used to calculate the physical properties of interest of the compounds.

The separation energy between the core and the valence was assumed to be − 8 Ry to avoid electron leakage. The theoretical equilibrium lattice parameters for the most stable structure of the MTO compound as a function of the chosen embedded potential, which includes exchange–correlation effects in Wien2k, were calculated using the

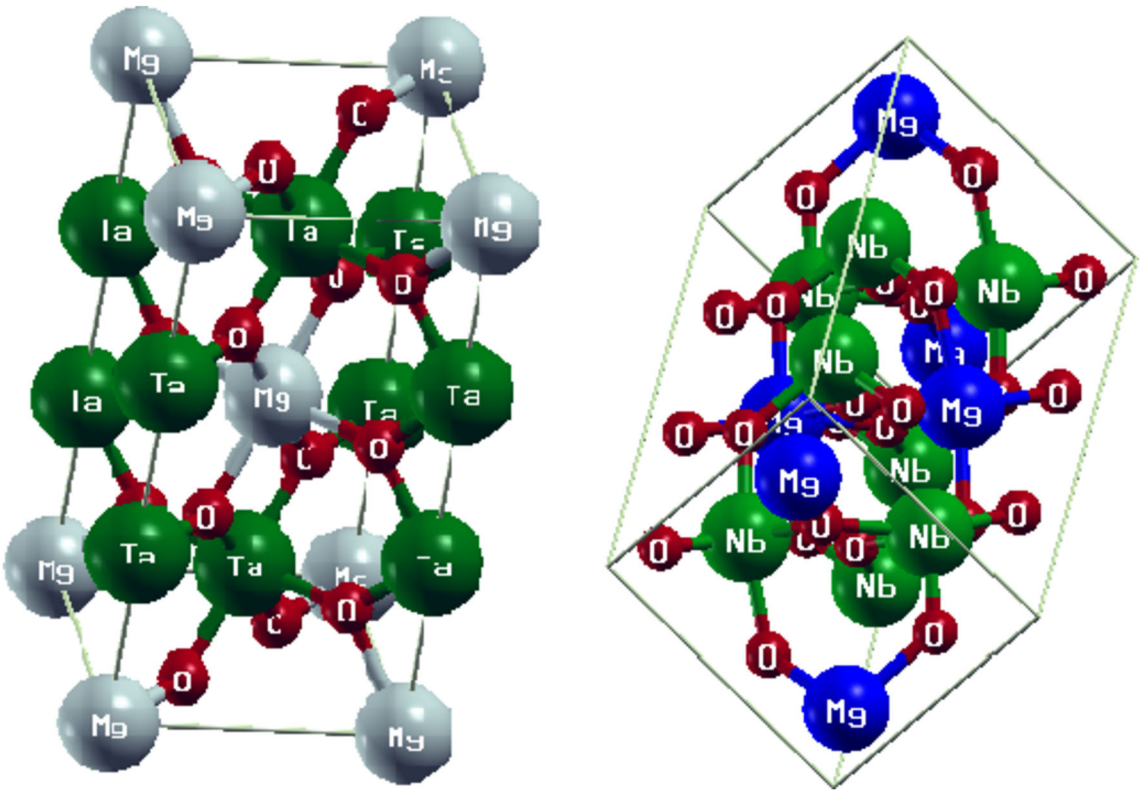

Fig. 1 Unit cell of (**a**) $MgTa_2O_6$ and (**b**) $MgNb_2O_6$ crystals

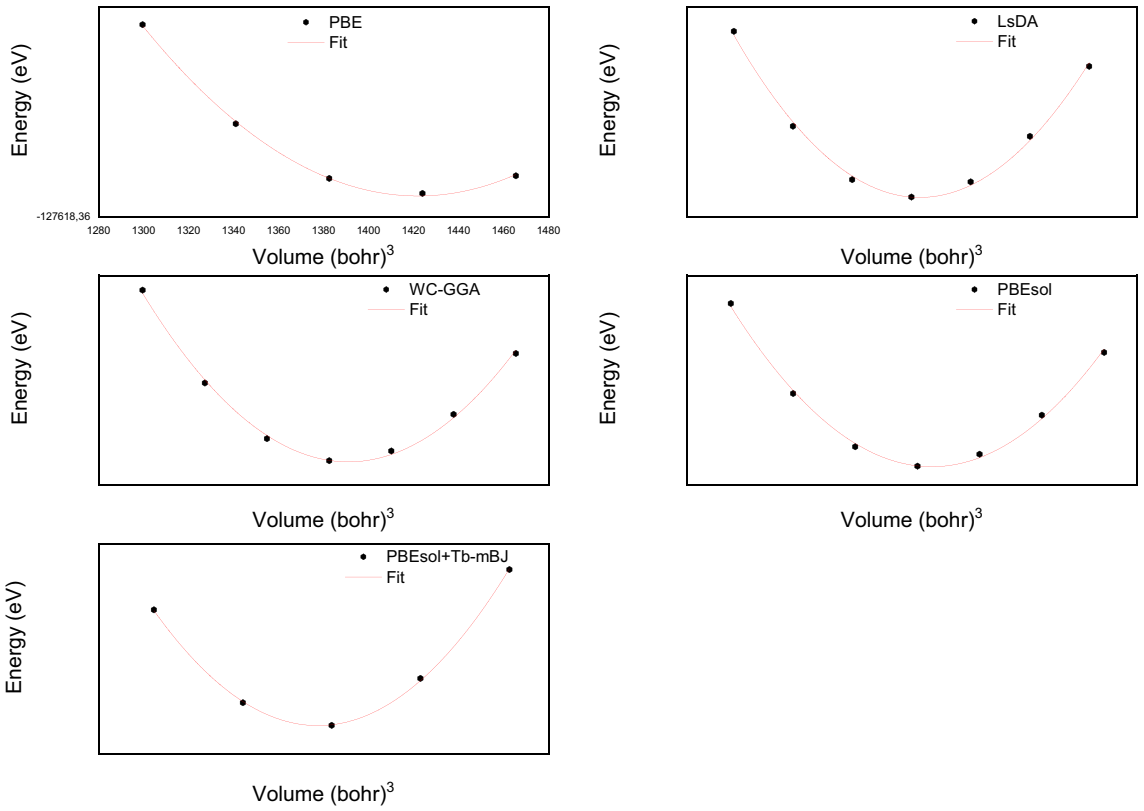

Fig. 2 Volume optimization of $MgTa_2O_6$ compound depending on selected potential (**a**) PBE (**b**) LsDA (**c**) WC-GGA (**d**) PBEsol-GGA and (**e**) TB-mBJ

Table 1 the equilibrium theoretical lattice parameters of MTO depending on the selected potential for including exchange–correlation effects

Lattice parameters (Å)	Experimental findings* (Å)	PBE-GGA (Å)	LSDA (Å)	WC-GGA (Å)	PBEsol-GGA (Å)	TB-mBJ + PBEsol
a	**4.7189**	4.765	4.718	4.720	4.719	**4.7188**
b	**4.7189**	4.765	4.718	4.720	4.719	**4.7188**
c	**9.2002**	9.292	9.221	9.215	9.210	**9.2001**

*Initial parameters were taken from [47]

volume optimization method (Fig. 2). The obtained results were compared with the available experimental data (Table 1) to select the best potential to be used for the rest of the calculation. It can be seen from Table 1 that PBEsol-GGA provides the best lattice parameters. However, it is a well-known fact that GGA underestimates the value of the band gap of the compound due to its nature [51]. Therefore, TB-mBJ potential [52] was used to obtain better results for the band gap value. In addition, the obtained lattice parameters for TB-mBJ + PBEsol are reported in Table 1 and 2 with the theoretically obtained lattice parameters depending on the potential used for the exchange–correlation effect. After selecting the potential for the exchange–correlation effect and optimizing the initial parameters for MTO, the same potential and initial parameters were used for MNO to be consistent in the calculation of the electronic band structure, density of states, etc.

The electronic configuration of systems is Mg [Ne] $3s^2$, O[He] $2s^2$ $2p^4$, Ta[Xe] $5d^4$ $6s^1$, and Nb[Kr] $4d^4$ $5s^1$. Sampling of the Brillouin zone was performed according to the Monkhorst–Pack scheme, using 63 k points [shell (12, 12, 6)] in the irreducible wedge of the zone.

In ABINIT calculation [50], a self-consistent, norm-conserving pseudopotential of Troullier–Martins type [53] produced by the FHI (FHI98PP) code [54] was used. For this calculation, the valence electrons were taken as follows $3s^2$ for Mg, $5d^3$ $6s^2$ for Ta, $4d^3$ $5s^2$ for Nb, and $2s^2$ $2p^4$ for O atom. All calculations were performed based on local density approximation (LDA) for the solution of the Kohn–Sham equation [55]. Twenty Hartree for cutoff energy and

Table 2 the equilibrium theoretical lattice parameters of MNO depending on the selected potential for including exchange–correlation effects

Lattice parameters Å	Experimental findings* (Å)	PBEsol-GGA Å	TB-mBJ + PBEsol
a	**14.1875**	14.4657	**14.1874**
b	**5.7001**	5.8110	**5.7000**
c	**5.0331**	5.1318	**5.0330**

*Initial parameters were taken from [15]

4 × 4 × 4 Monkhorts–Pack mesh grid for the Brillouin zone were selected. The properties of the sample were obtained after geometry optimization.

The optical properties of the investigated compounds are calculated by the frequency-dependent dielectric function (FDDF), $\varepsilon(\omega)$, given by

$$\varepsilon(\omega) = \varepsilon_1(\omega) + i\varepsilon_2(\omega) \tag{1}$$

In this equation, $\varepsilon_1(\omega)$ represents the real part of the FDDF and $\varepsilon_2(\omega)$ stands for the imaginary part of the FDDF. While $\varepsilon_1(\omega)$ could be obtained from $\varepsilon_2(\omega)$ with Kramers–Kroning relations, $\varepsilon_2(\omega)$ is extracted from electronic structure calculation using the joint density of states and optical matrix elements. The equations for the real and imaginary parts of the FDDF are given by [56]

$$\varepsilon_1(\omega) = 1 + \frac{2}{\pi}\int_0^{\infty} \frac{\varepsilon_2(\omega')\omega' d\omega'}{\omega'^2 - \omega^2} \tag{2}$$

$$\varepsilon_2(\omega) = \frac{Ve^2}{2\pi m^2\omega^2}\int d^3k \sum_{nn'} |kn|p|kn'|^2 \times f(kn)(1 - f(kn'))\partial(E_{kn} - E_{kn'} - \hbar\omega) \tag{3}$$

p is the momentum operator between the states n and n', the electronic charge is represented by e, m stands for the mass of an electron, photon energy is presented by ω, V is the volume, $f(kn)$ is the Fermi distribution function, and $|kn\rangle$ stands for eigenfunction with the eigenvalue of E_{kn}. The other optical properties can be obtained using real and imaginary parts of FDDF.

Wien2k needs an additional program to calculate the elastic properties of any compounds. Therefore, we decided to employ ABINIT code to calculate the elastic properties of compounds instead of using extra code with Wien2k.

Results and discussion

In this section, the theoretical investigation of the structural, electronic, optical, and elastic properties of MXO (X = Ta, Nb) compounds was evaluated.

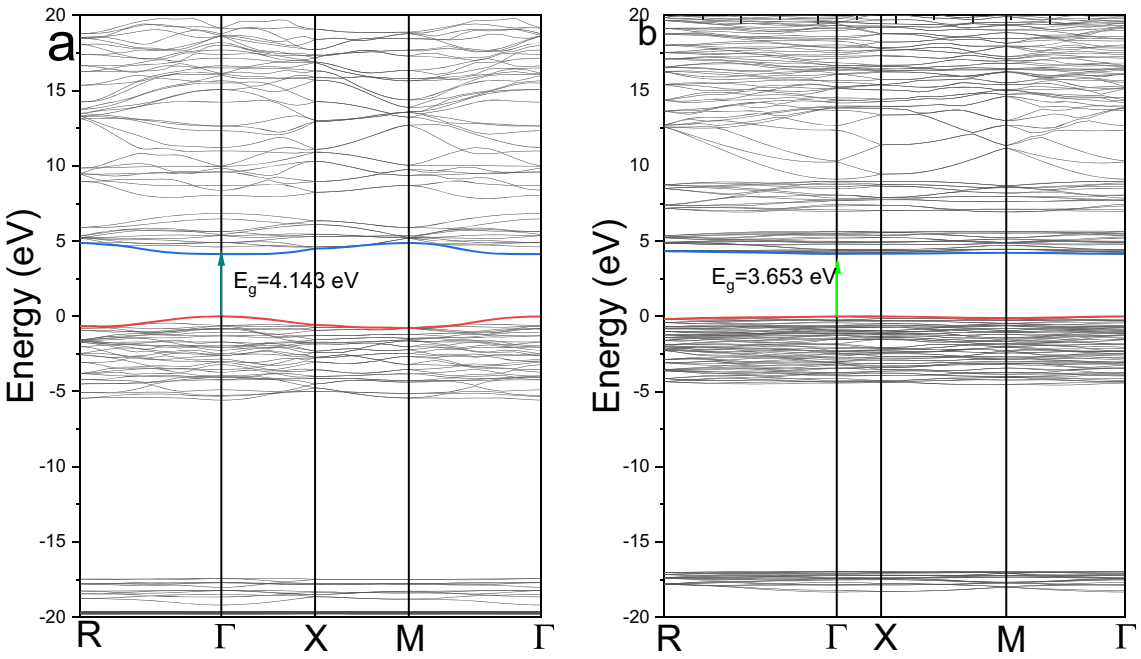

Fig. 3 Electronic band structure of (**a**) MTO (**b**) MNO

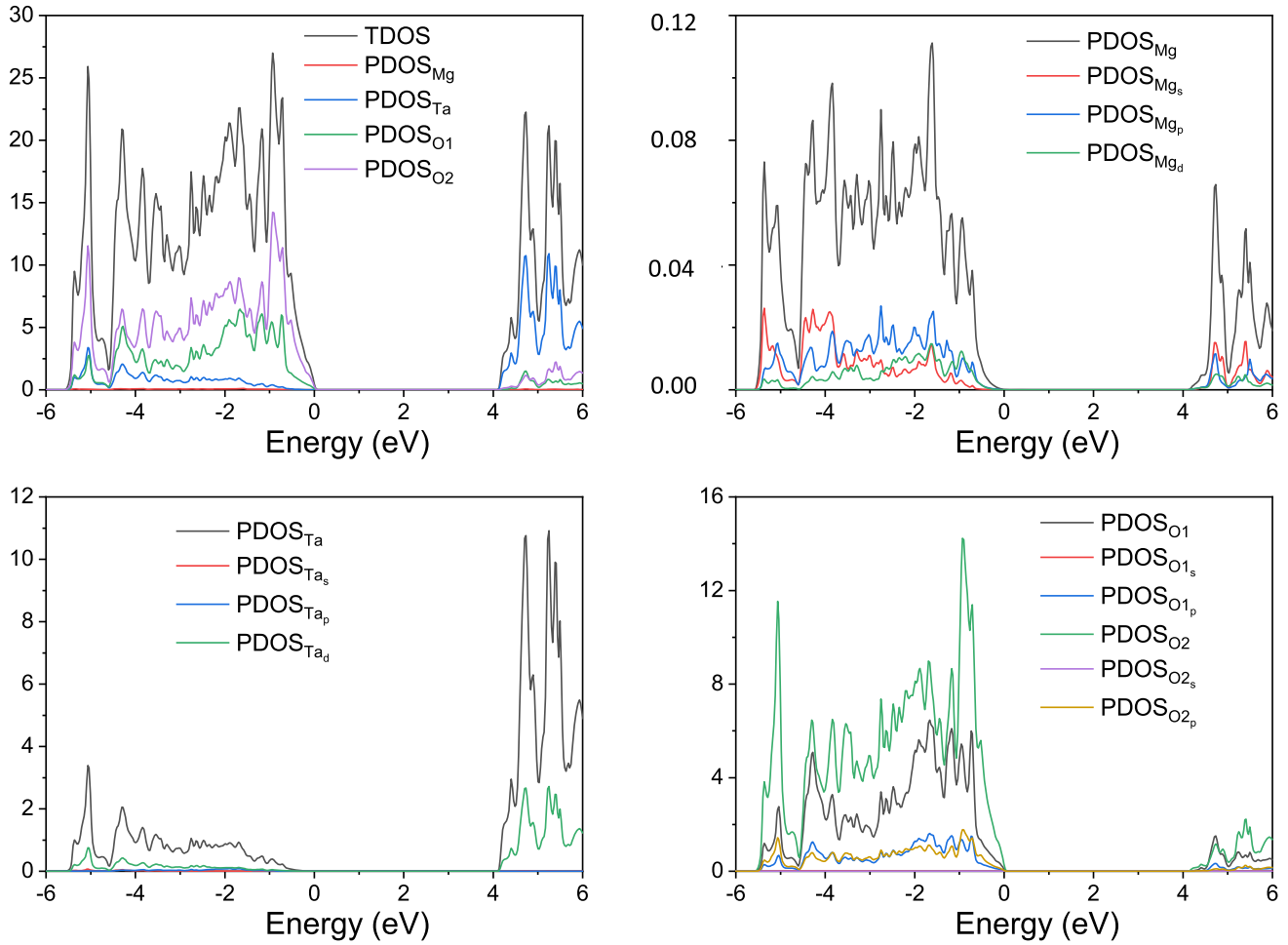

Fig. 4 Total and partial density of states of MTO

Electronic band structure

Figure 3 shows the band structure of TB-mBJ + PBEsol (hereafter TB-mBJ) for compounds at equilibrium (to our knowledge, TB-mBJ band structures have not been reported). The position of the valence band maximum (at Γ) and the conduction band minimum (at Γ) to E_F results in band gaps and implies a direct transition for both compounds. The calculated value of the band gap is 4.143 eV for MTO and 3.653 eV for MNO which is in good agreement with previous studies[41, 42, 57, 58]. The band gap value tells us that these materials have semiconducting behavior and the energy band gap increases with increasing the atomic number (the atomic number of Ta is higher than of Nb). We would like to emphasize that direct transition is favorable for optoelectronics applications due to avoiding the energy loss by lattice vibrations, and semiconductor nature.

The contribution of the partial (*s*, *p*, *d*-states) and total density of states (DOS) of the constituent elements (Mg, O, Ta, and Nb) is depicted in Figs. 4 and 5. The first glance indicates that nolocalized energy states have crossed the Fermi level. Moreover, there is a significant gap between the valence and conduction bands in both cases. The overall shapes of the two compounds studied are similar and show only minor differences in the position of the states and the intensities.

The Mg contribution to the DOS is not only in the valence band but also in the conduction band. Compared to Ta/Nb and O atoms, however, the Mg contribution can be neglected. While the DOS of the O atom is mainly dominated by the 2*p* states in the valence band, the DOS of the Nb/Ta atom consists predominantly of 5*d*/4*d* states in the conduction band. This implies the transition from O_{2p} to $Ta/Nb_{5d/4d}$.

Linear optical properties

For optoelectronic and photovoltaic technologies, it is necessary to calculate the optical properties of compounds, which provide information about occupied and unoccupied

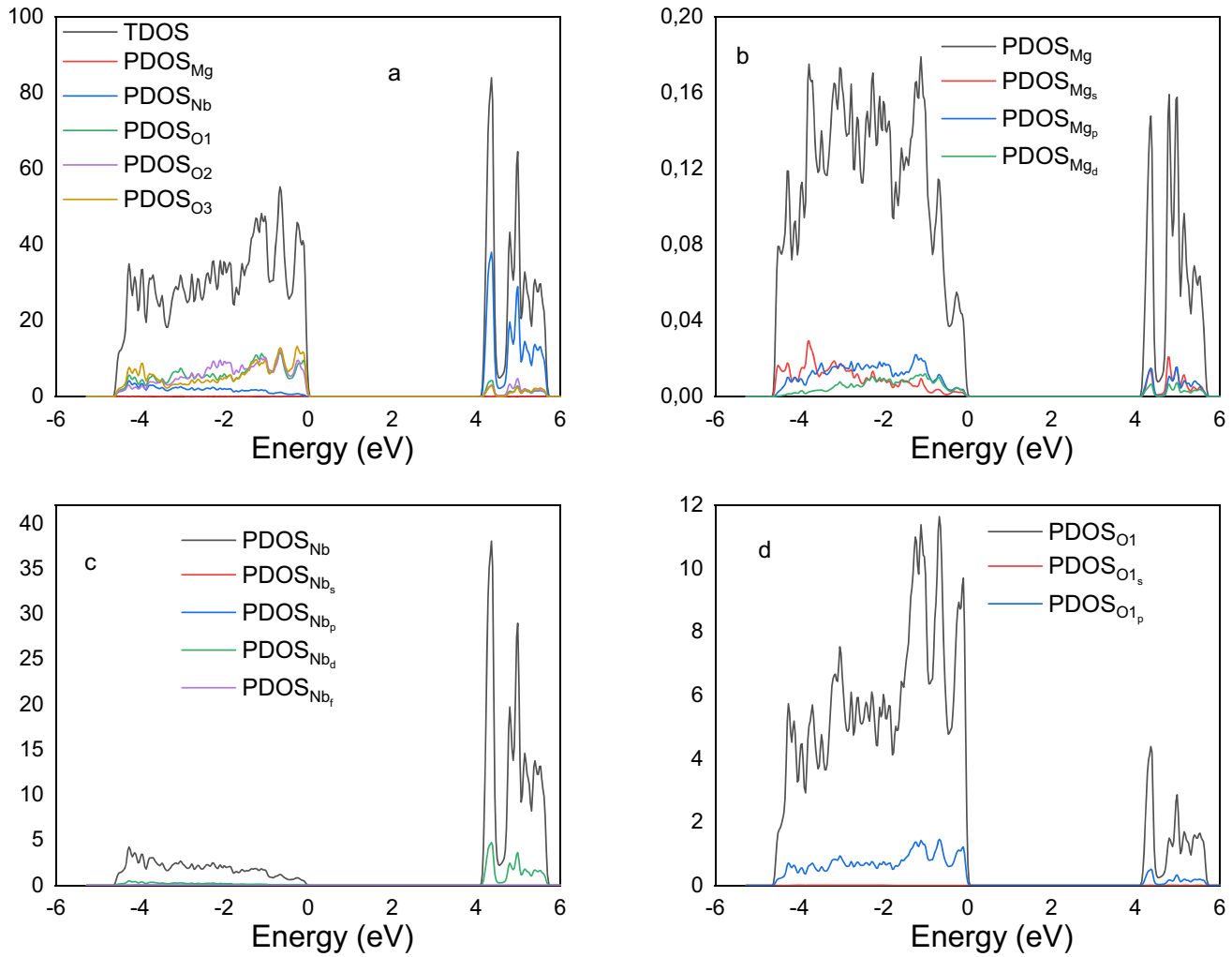

Fig. 5 Total and partial density of states of MNO

states [59]. Depending on the studied compound, $\varepsilon_x(\omega)$, $\varepsilon_y(\omega)$, and $\varepsilon_z(\omega)$ components of the dielectric tensor were calculated and discussed.

It is a well-known fact that the optical constant is the response of the material to incident electromagnetic radiation and the axis-dependent optical constants of MXO (X = Ta, Nb) could be calculated via the real, which is related to the dispersive conduct of material, and the imaginary part, which corresponds to the absorbing behavior of the material, of the frequency-dependent dielectric function (FDDF). All calculated real and imaginary parts of FDDF for both compounds are given in the photon energy 0–40 eV and illustrated in Fig. 6 (a–d).

In the imaginary part, $\varepsilon_2(w)$, the threshold energy of the dielectric function is around $E_0 = 4.12$ eV for MTO and $E_0 = 3.60$ eV for MNO, which corresponds to the fundamental band gap at equilibrium. Both materials are good candidates for applications in the UV region of the spectrum with larger band gap values [60].

From the imaginary part of the FDDF, it is obvious that there is a strong absorption peak in the range of 4–20 eV and 3.5–22 eV for MTO and MNO, respectively. The maximum absorption peak is located at 10.89 eV for MTO and 5.56 eV for MNO. These peaks are responsible for the transition from the valence band to the unoccupied conduction band.

The static value of the axis-dependent real part of FDDF $\varepsilon_{1x} = \varepsilon_{1y} = 3.33$ and $\varepsilon_{1z} = 3.58$ for MTO and $\varepsilon_{1x} = 4.37$, $\varepsilon_{1y} = 4.07$, and $\varepsilon_{1z} = 4.53$ for MNO. From the zero frequency limit, they start to increase and reach the maximum value around 5.02 eV for MTO and 4.39 eV for MNO, and then go into the negative range for 11.29–13.22 eV, 19.95–21.90 eV and 39.50–… eV for MTO and 9.21–12.25 eV, 20.28–24.19 eV, and 35.9–36.78 eV for MNO. At the negative value of the real part of the FDDF, the materials behave like metal and reflect all incident electromagnetic radiation. In addition, Fig. 6 shows a

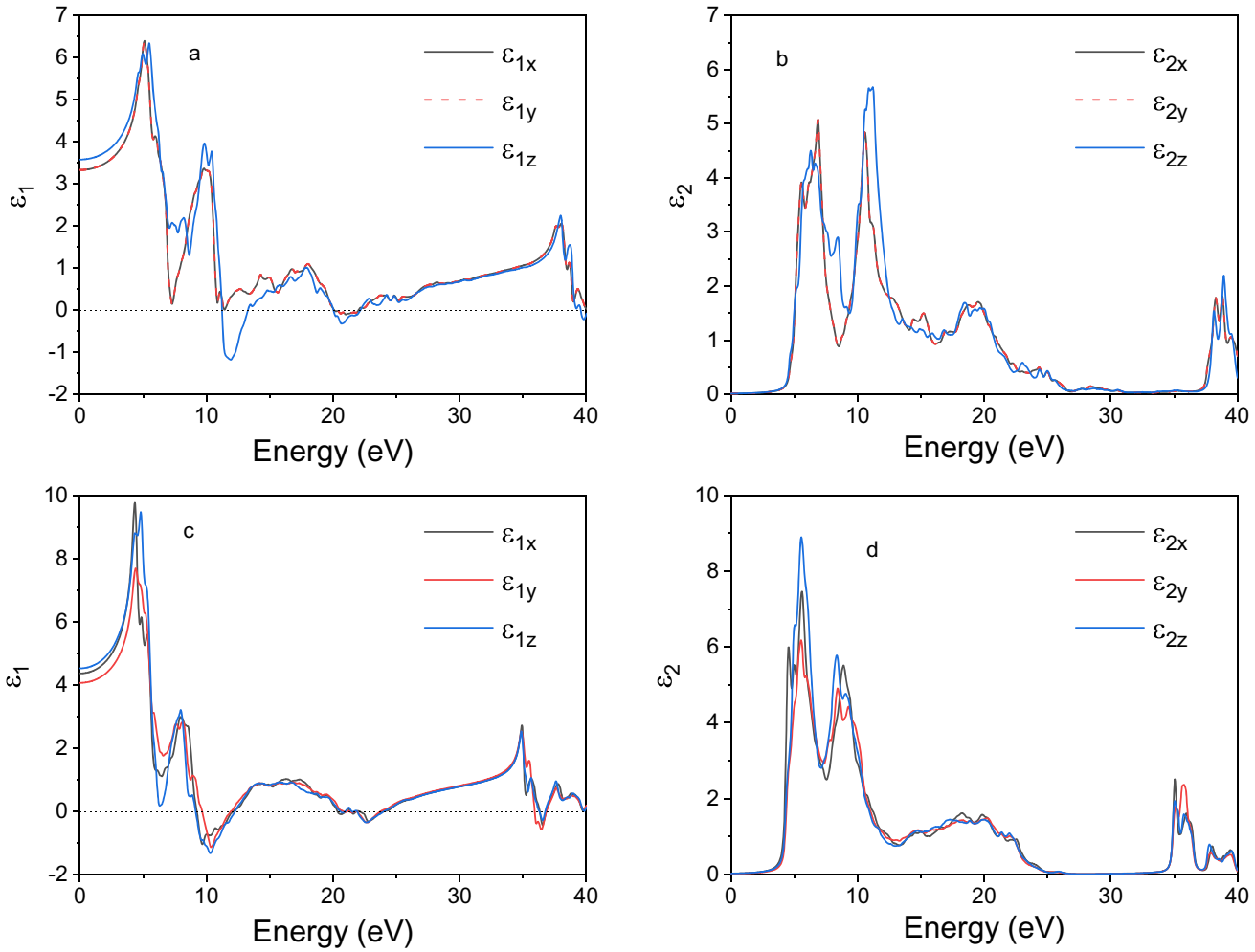

Fig. 6 Calculated plots of (**a**) real part of MTO (**b**) imaginary part of MTO (**c**) real part of MNO (**d**) imaginary part of MNO

considerable anisotropy between the spectra, implying a different polarization for this compound.

Figure 7 (a–d) represents the refractive index and extinction coefficients of compounds. The calculated axis dependent static refractive index, $n_i(0)$ $i = x,y,z$, is 1.82, 1.82, and 1.89 and 2.10, 2.02, and 2.12 for MTO and MNO, respectively. It increases with the energy in the transparent region. As can be seen from Fig. 7 (a and c), the axis-dependent refractive index is greater than unity meaning photons, which enter a material, are slowed down by interaction between photons and electrons. Due to the low refractive index of both materials, they can be used in optical reflector technology[61].

The maximum peaks of the extinction coefficient (Fig. 7(b and d)), which describes the absorption of optical energy in the optical medium during light transmission, are in the energy range of 5–10 eV. The characteristic analysis of the extinction coefficient shows similarity with the imaginary part of the dielectric function. In addition, both compounds have significant values in the UV region. This shows that both compounds are very important materials for optoelectronic applications.

The optical absorption coefficient and the conductivity are presented in (Fig. 8). The conduction of emitted electrons is represented by the optical conductivity. A high value of optical conductivity in the visible range is desired for the application of solar cells. As can be seen in Fig. 8 (a and d), both compounds have a low optical conductivity in the visible light range (1.87–3.8 eV) which makes the compounds a poor candidate for use in the solar cell application. However, with band engineering, a compound with a wide band gap could be used for solar cell application.

Absorption contains information about how the material behaves when interacting with radiation and indicates the ability of each material to absorb indecent photons of a certain energy. Absorption starts at 4.45 eV (Fig. 8 c) and 3.65 eV (Fig. 8 f) for MTO and MNO, respectively. Beyond that, there is no absorption after 350 nm which implies that material absorbs incoming photons in the UV

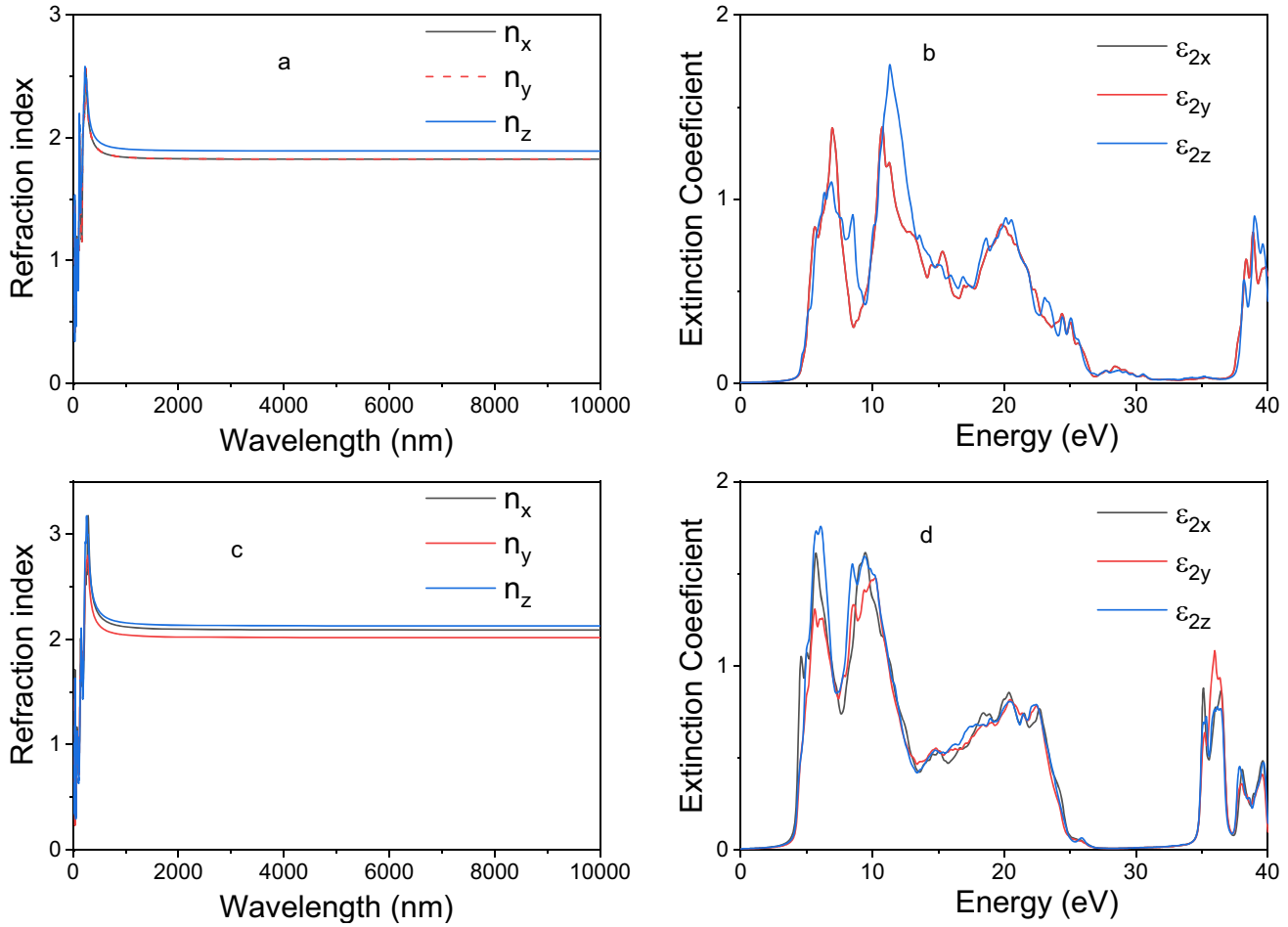

Fig. 7 Calculated plots of (**a**) refractive index of MTO (**b**) extinction coefficient of MTO (**c**) refractive index part of MNO (**d**) extinction coefficient of MNO

range. Furthermore, the calculated optical absorption coefficient of the compounds is about 10^5 cm^{-1} which makes the compound a good candidate for optoelectronic applications (Fig. 8 b and f).

Mechanical properties

To obtain the response of the material to external stresses in the elastic limit, it is necessary to compute the elastic constants, C_{ij}, [62]. Elastic constants define the behavior of a solid that undergoes stress, deforms, and then returns to its original shape [63, 64]. ABINIT code was used to obtain a set of the zero-pressure elastic constants for both compounds. In addition, the obtained elastic constants are used to check the mechanical stability of compounds.

The number of elastic constants is reduced due to the crystal symmetry: nine independent elastic constants, (C_{11}, C_{12}, C_{13}, C_{22}, C_{23}, C_{33}, C_{44}, C_{55}, and C_{66}), for orthorhombic MNO and six independent elastic constants, (C_{11}, C_{12}, C_{13}, C_{33}, C_{44}, and C_{66}), for tetragonal MTO. Table 1 shows the calculated elastic constants for the compounds.

The calculated elastic constants are inserted in Table 2. The obtained elastic constant should satisfy the Born stability criteria for mechanical stability [65]:

Orthorhombic stability criteria are given below

$$C_{11} > 0, C_{22} > 0, C_{33} > 0, C_{44} > 0, C_{55} > 0 \text{ and } C_{66} > 0$$
$$\{C_{11} + C_{22} + C_{33} + 2(C_{12} + C_{13})\} > 0$$
$$\{C_{11} + C_{22} - 2C_{12}\} > 0$$
$$\{C_{11} + C_{33} - 2C_{13}\} > 0$$
$$\{C_{22} + C_{33} - 2C_{23}\} > 0$$

Tetragonal stability criteria are the following

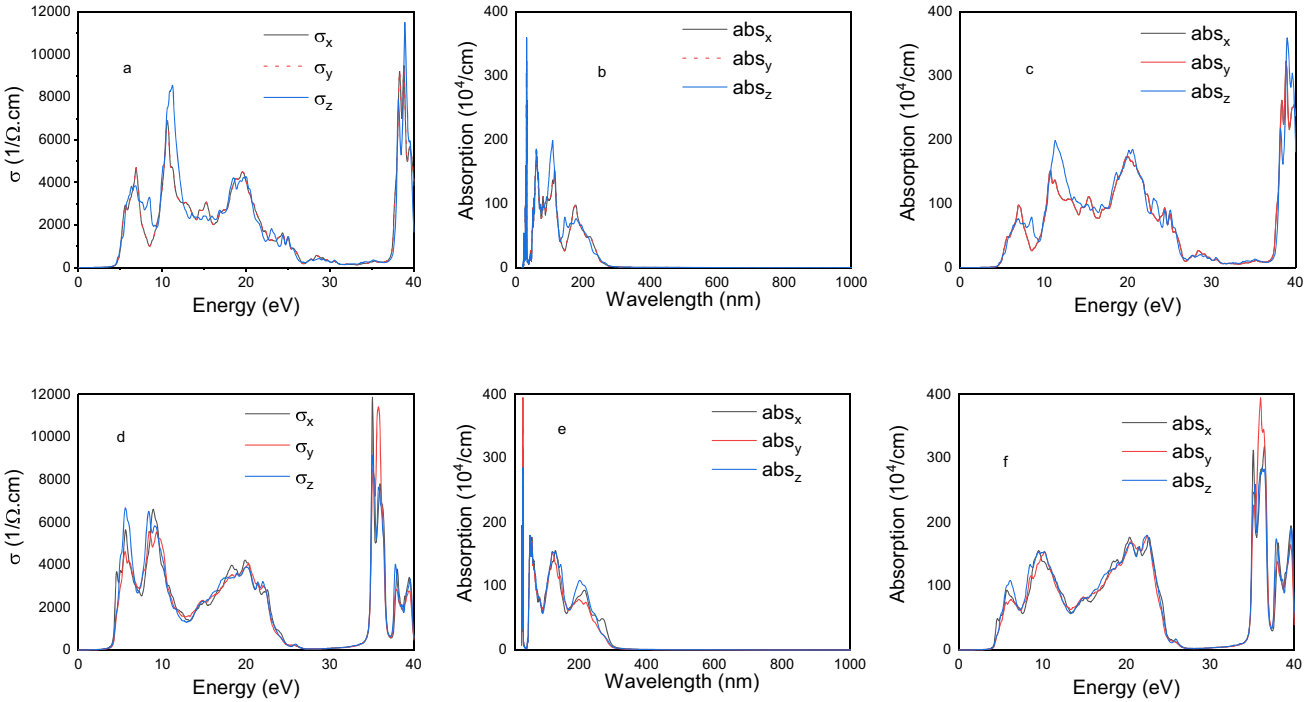

Fig. 8 Calculated axes dependent optical conductivity of (**a**) MTO (**d**) MNO. Calculated optical absorption for *xx*, *yy*, and *zz* directions (**b**) and (**c**) for MTO (**e**) and (**f**) for MNO

Table 3 Calculated single-crystal elastic constants and the elastic compliance constants for the MXO compound

Compound	Elastic constants (GPa)								
	C_{11}	C_{22}	C_{33}	C_{44}	C_{55}	C_{66}	C_{12}	C_{13}	C_{23}
$MgTa_2O_6$	528.976	–	635.089	209.333	–	278.442	235.689	223.205	–
$MgNb_2O_6$	384.385	416.086	450.652	137.754	216.201	203.784	214.503	215.000	168.347

$$C_{11} > 0, C_{33} > 0, C_{44} > 0 \text{ and } C_{66} > 0$$
$$\{C_{11} - C_{12}\} > 0 \text{ and } \{C_{11} + C_{33} - 2C_{13}\} > 0$$
$$\{2(C_{11} + C_{12}) + C_{33} + 4C_{13}\} > 0$$

According to the inserted values in Table 3 and the Born stability criteria, both compounds are mechanically stable at ambient pressure.

From the calculated elastic constant and using the Voight and Reuss approximation, bulk modulus (B), and shear modulus (G), which stand for resistance of a solid against volume and shape change, respectively, are calculated using the common relations given in [66, 67] and inserted in Table 4.

The calculated value of bulk modulus and shear modulus of MTO is smaller than the calculated values of XTa_2O_6 (X = Ca, Sr) [67, 68], which implies that MTO is a much more compressible compound than both compounds. However, no information is available for MNO, we could not make a comparison. In addition, MNO has a lower bulk and shear modulus than MTO, which means that MNO is a much more compressible compound. The calculated Young modulus, (268.099 GPa for MTO) and (373.134 GPa for MNO), implies the low stiffness character of the compound. The compounds are classified according to the value of the Poisson ratio (Pr). The value of Pr equals 0.1 for covalent materials, 0.25 for ionic materials, and 0.33 for metallic materials. The calculated Pr of MTO is 0.251 and of MNO is 0.271. Both compounds have metallic characteristics, and the atomic bonding is ionic type. The ductile properties of materials could be revealed by Pugh's criterion [69]. If the flexibility coefficient is smaller than 1.75,

Table 4 The calculated isotropic bulk modulus, shear modulus, Young's modulus, Poisson ratio, flexibility coefficient, Debye temperature, the average elastic, and longitudinal and transverse sound wave velocities

Property	Symbol (unit)	Value	
		$MgTa_2O_6$	$MgNb_2O_6$
Voight bulk modulus	$\boldsymbol{B_V}$ (GPa)	339.693	271.869
Reuss bulk modulus	$\boldsymbol{B_R}$ (GPa)	337.988	271.611
Bulk modulus VRH average	$\boldsymbol{B_{VRH}}$ (GPa)	338.840	271.740
Voight shear modulus	$\boldsymbol{G_V}$ (GPa)	206.818	155.100
Reuss shear modulus	$\boldsymbol{G_R}$ (GPa)	198.058	138.442
Shear modulus VRH average	$\boldsymbol{G_{VRH}}$ (GPa)	202.438	146.771
Young modulus	$\boldsymbol{E}$ (GPa)	506.454	373.134
Poisson ratio	$\boldsymbol{v}$ (–)	0.251	0.271
Flexibility coefficient	**K** (–)	1.674	1.851
Shear anisotropic factor	$\boldsymbol{A}_{\{100\}}$	1.793	1.362
Shear anisotropic factor	$\boldsymbol{A}_{\{010\}}$	1.793	1.633
Shear anisotropic factor	$\boldsymbol{A}_{\{001\}}$	1.89	2.194
Shear anisotropic factor	$\boldsymbol{A}_{\{1\bar{1}0\}}$	0.97	–
Universal elastic anisotropy index	$\boldsymbol{A^U}$	0.23	0.60
Percent compressible anisotropy	$A_{comp}(\%)$	0.2	0.4
Percent shear anisotropy	$A_{shear}(\%)$	2.1	1.1

the materials are classified as brittle materials; otherwise, the material belongs to the ductile materials. The calculated value of the flexibility coefficient is 2.55 and 1.851 for MTO and MNO, respectively. According to the findings, both materials are ductile.

The elastic anisotropy related to the elastic properties of compounds helps to calculate the bonding nature and microcracks formation in materials [70]. The universal elastic anisotropic index, A^U, percent shear anisotropy, A_{shear}, and percent compressible, A_{comp}, describe the elastic anisotropy of a solid [71]. In addition, the shear anisotropy (A_{100}, A_{010}, $A_{1\bar{1}0}$ and A_{001}) also needs to be calculated to describe the elastic modulus anisotropy of investigated compounds depending on the structure type. Due to the tetragonal and orthorhombic structures of investigated compounds, the given formula in [71, 72] was used and the obtained results are inserted in Table 3. If $A^U = A_{shear} = A_{comp}$ is equal to zero and $A_{100} = A_{010} = A_{001}$ equal to unity means the solid presents elastically isotropic. A solid cannot satisfy elastically conditions, and it is said that a solid is elastically anisotropic. According to Table 3, the values reflect the elastic anisotropy for both compounds.

Conclusion

In summary, we reported the theoretical calculation of the electronic, structural, optical, and elastic properties of MgX_2O_6 (X = Ta, Nb) compounds based on first-principles calculations. The results reveal that both compounds are classified as semiconductor materials with a wide band gap, which is in the visible region and is sought for optoelectronic applications. Furthermore, the band gap structure calculation shows a direct transition at Γ high symmetry point for both compounds. The investigated optical properties will help researchers understand the electro-optical conduct of the two analyzed compounds. The PDOS results show that while Mg contribution to the bands could be neglected compared to others, the main contributions of the O-2*p*, Nb-4*d*, and Ta-5*d* orbitals enhance the electronic behavior of these materials. The elastic constant based on the Vioght-Reuss approximation has confirmed the mechanical stability of these compounds, which are found to be ductile, anisotropic, and exhibit ionic features. The optical properties such as reflectivity, refractivity, absorption coefficient, and optical conductivity were calculated and explained in detail. The performed calculation will be a guide for future studies related to these compounds.

Funding Open access funding provided by the Scientific and Technological Research Council of Türkiye (TÜBİTAK).

References

[1] H P Beck, H Seup-Ra, R Haberkorn, H Kohlmann, M Eul, T Harmening and R. Pöttgen (2010)
[2] H P Beck *Zeitschrift Für Krist. - Cryst. Mater.* **227** 843 (2012)
[3] H P Beck *Zeitschrift Für Krist.—Cryst. Mater.* **228** 271 (2013)
[4] C Tealdi, M Saiful Islam, L Malavasi and G Flor *J. Solid State Chem.* **177** 4359 (2004)
[5] C R Ferrari and A C Hernandes *J. Eur. Ceram. Soc.* **22** 2101 (2002)
[6] S Jia, Q Zhou, F Huang, F Li, Y Hu, L Huang, L Li, Y Li and T Cui AIP Adv. **10** (2020)
[7] C L Huang, K H Chiang and C Y Huang *Mater. Chem. Phys.* **90** 373 (2005)
[8] F Emmenegger *J. Cryst. Growth* **3–4** 135 (1968)
[9] M Greenblatt, B M Wanklyn and B J Garrard *J. Cryst. Growth* **58** 463 (1982)
[10] G Blasse, G J Dirksen and L H Brixner *Mater. Chem. Phys.* **14** 485 (1986)
[11] H S Horowitz J. Am. Ceram. Soc. **71**, C-250 (1988)
[12] M Higuchi, K Ando, J Takahashi and K Kodaira *J. Ceram. Soc. Japan* **101** 118 (1993)
[13] K Polgár, A Péter, J Paitz and C Zaldo *J. Cryst. Growth* **151** 365 (1995)
[14] P McBride, R Sherlock, T J Glynn and G Walker *J. Appl. Spectrosc.* **62** 636 (1995)
[15] S Ananta, R Brydson and N W Thomas *J. Eur. Ceram. Soc.* **19** 355 (1999)
[16] N K Kim *Mater. Lett.* **32** 127 (1997)
[17] K Sreedhar and A Mitra *Mater. Res. Bull.* **32** 1643 (1997)
[18] E R Camargo, E Longo and E R Leite *J. Sol-Gel Sci. Technol.* **17** 111 (2000)
[19] D Bravo, K Polgár and F J López *Solid State Commun.* **103** 65 (1997)
[20] A Mergen *Ceram. Int.* **35** 1151 (2009)
[21] Y Zhang, B Fu, Y Liu, X Wang, T Li and Z Yue *J. Alloys Compd.* **505** 750 (2010)
[22] Y Zhang, X Zhou and X Wang *J. Sol-Gel Sci. Technol.* **50** 348 (2009)
[23] S Nangia, M Thirumal, A K Ganguli and P L Gai *Microsc. Microanal.* **8** 1414 (2002)
[24] L Li, G Feng, D Wang, H Yang, Z Gao, B Li, D Xu, Z Ding and X Liu *J. Alloys Compd.* **509** L263 (2011)
[25] V Shanker and A K Ganguli *Bull. Mater. Sci.* **26** 741 (2003)
[26] L Abdul Khalam, S Thomas, and M T Sebastian Int. J. Appl. Ceram. Technol. **4** 359 (2007)
[27] T H Fang, Y J Hsiao, Y S Chang, L W Ji and S H Kang *Curr. Opin. Solid State Mater. Sci.* **12** 51 (2008)
[28] C S Hsu, C L Huang, J F Tseng and C Y Huang *Mater. Res. Bull.* **38** 1091 (2003)
[29] C-H Hsu, C-F Tseng and C-L Huang *Jpn. J. Appl. Phys.* **44** 8043 (2005)
[30] H T Wu, Y S Jiang and Y L Yue *Ceram. Int.* **38** 5151 (2012)
[31] B J Fu, Y C Zhang, X L Su, Y H Liu and M Hong *Key Eng. Mater.* **512–515** 1222 (2012)
[32] M Dang, H Lin, X Yao, H Ren, T Xie, H Peng and Z Tan *Ceram. Int.* **45** 24244 (2019)
[33] L Shi, X Wang, R Peng, Y Lu, C Liu, D Zhang and H Zhang *Ceram. Int.* **48** 20096 (2022)
[34] S Wang, A Yang, S Jiang, H Ren, T Xie, H Peng, X Yao and H Lin *J. Mater. Sci. Mater. Electron.* **32** 24320 (2021)
[35] J Huang, Y Li, K Li, Y Sun, Z Shen and Z Wang *J. Mater. Sci. Mater. Electron.* **33** 27014 (2022)
[36] J Y Si, S Y Song, N Liu, G M Cai and L M Su *J. Lumin.* **198** 10 (2018)
[37] L P S Santos, L S Cavalcante, M T Fabbro, H Beltrán Mir, E Cordoncillo, J Andrés, and E Longo, Superlattices Microstruct. **79** 180 (2015)
[38] D V Mlotswa, V R Orante-Barrón, B M Mothudi, S J Mofokeng, G N Ngubeni, D Poelman and L L Noto *J. Lumin.* **252** 119375 (2022)
[39] M Birdeanu, M Vaida and E Fagadar-Cosma *Manuf. Rev.* **7** 39 (2020)
[40] K D Miller and J M Rondinelli *Phys. Rev. Mater.* **6** 75007 (2022)
[41] L Huang, Q Zhou, F Li and L Li *Mod. Phys. Lett. B* **34** 2050281 (2020)
[42] N Basavaraju, S C Prashantha, B S Surendra, T R Shashi Shekhar, M R Anil Kumar, C R Ravikumar, N Raghavendra and T S Shashidhara Environ. Nanotechnology, Monit. Manag. **16** 100581 (2021)
[43] N Basavaraju, S C Prashantha, H Nagabhushana, M Chandrasekhar, A N Kumar, T R S Shekhar, S Ashwini and K S Anantharaju *Ceram. Int.* **47** 14899 (2021)
[44] N Basavaraju, S C Prashantha, H Nagabhushana, C Pratapkumar, C R Ravikumar, M R A Kumar, B S Surendra, T R S Shekhar, H B Premkumar and H P Nagaswarupa *Ceram. Int.* **47** 10370 (2021)
[45] S C Navale and V Ravi *Mater. Sci. Eng. B* **119** 189 (2005)
[46] K N Singh and P K Bajpai *Phys. B Condens. Matter* **405** 303 (2010)
[47] D Xu, S Gao, W Liu, Y Liu, Q Zhou, L Li, T Cui and H Yuan (2019)
[48] S C Navale, A B Gaikwad and V Ravi *Mater. Res. Bull.* **41** 1353 (2006)
[49] P Blaha, K Schwarz, F Tran, R Laskowski, G K H Madsen and L D Marks *J. Chem. Phys.* **152** 74101 (2020)
[50] X Gonze, B Amadon, P-M Anglade, J-M Beuken, F Bottin, P Boulanger, F Bruneval, D Caliste, R Caracas, M Côté, T Deutsch, L Genovese, P Ghosez, M Giantomassi, S Goedecker, D Hamann, P Hermet, F Jollet, G Jomard and J Zwanziger *Comput. Phys. Commun.* **180** 2582 (2009)
[51] S Picozzi, A Continenza and A J Freeman *Phys. Rev. B* **66** 94421 (2002)
[52] F Tran and P Blaha *Phys. Rev. Lett.* **102** 226401 (2009)
[53] N Troullier and J L Martins *Phys. Rev. B* **43** 1993 (1991)
[54] M Fuchs and M Scheffler *Comput. Phys. Commun.* **119** 67 (1999)
[55] W Kohn and L J Sham *Phys. Rev.* **140** A1133 (1965)
[56] N Boucerredj, K Beggas, Z Chouahda, S Ghemid and H Meradji Acta Phys. Pol. A. **138** (2020)
[57] J-M Wu, I Djerdj, T Graberg and B Smarsly *Beilstein J. Nanotechnol.* **3** 123 (2012)
[58] H Aycibin *Process. Appl. Ceram.* **17** 1 (2023)
[59] A G Petukhov, I I Mazin, L Chioncel and A I Lichtenstein *Phys. Rev. B* **67** 153106 (2003)

[60] M Maqbool M Kordesch and A Kayani J. Opt. Soc. Am. B-Opt. Phys. - J OPT SOC AM B-OPT Phys. **26** (2009)
[61] E F Schubert, J K Kim and J-Q Xi *Phys. Status Solidi* **244** 3002 (2007)
[62] M de Jong, W Chen, T Angsten, A Jain, R Notestine, A Gamst, M Sluiter, C Krishna Ande, S van der Zwaag, J J Plata, C Toher, S Curtarolo, G Ceder, K A Persson and M Asta Sci. Data **2** 150009 (2015)
[63] S A Khandy, S G Vaid, I Islam, A K Hafiz and J Da Chai *J. Alloys Compd.* **867** 158966 (2021)
[64] S A Khandy Sci. Rep. **11** 20756 (123AD)
[65] M Born *Math. Proc. Cambridge Philos. Soc.* **36** 160 (1940)
[66] H Koc, A Yildirim, E Tetik and E Deligoz *Comput. Mater. Sci.* **62** 235 (2012)
[67] F Subhan, S Azam, G Khan, M Irfan, S Muhammad, A G Al-Sehemi, S H Naqib, R Khenata, S A Khan, I V Kityk and B Amin *J. Alloys Compd.* **785** 232 (2019)
[68] M Erzen, M Aycibin and H Akkus *Can. J. Phys.* **100** 519 (2022)
[69] S F Pugh *Dublin Philos. Mag. J. Sci.* **45** 823 (1954)
[70] S Simsek, H Koc, A Mamedov and E Ozbay *Ferroelectrics* **538** 135 (2019)
[71] W Bao, D Liu, P Li and Y Duan *Ceram. Int.* **45** 1857 (2019)
[72] Y Wu, Y Duan, X Wang, M Peng, L Shen and H Qi *Mater. Today Commun.* **33** 104651 (2022)